Tellus (1988), *40A*, 220–236

Finite amplitude stratified air flow past isolated mountains on an f-plane

By SIGURDUR THORSTEINSSON[1], *Institute of Geophysics, University of Oslo, P.O. Box 1022, Blindern, N-0315 Oslo 3, Norway*

(Manuscript received 6 February; in final form 11 June 1987)

ABSTRACT

A time-dependent non-linear model was employed to simulate the adiabatic hydrostatic flow of stably stratified air crossing an isolated orography on the f-plane. The potential vorticity of the air is specified as a positive function of its potential temperature. The numerical model integrations are performed on a limited area domain with locally-determined inflow/outflow side boundaries.

The results for nearly steady states have been obtained for a number of isolated mesoscale orographic phenomena—including flow splitting, wave amplitudes, low-level jets, strong downslope winds, and anomalously high temperatures behind the mountains. The flow pattern is considered in relation to different values for the Rossby number, Ro, and the non-dimensional mountain height, H, with the non-dimensional stability fixed. The study indicates that for a sufficiently large H and Ro, most of the low-level air is diverted around the mountain, and the downslope flow on the lee side originates from potentially warmer upwind strata above the surface. The maximum magnitude (in degrees) of this warm zone increases for constant values of H with increasing Ro, and also for constant values of Ro as H increases. The downstream extent of the zone is of the order of the Rossby radius of deformation corresponding to the height of the mountain. The location of the minimum and maximum wind speeds is most sensitive to the value of Ro, and their strength is most sensitive to H.

1. Introduction

The stationary flow over an infinite mountain ridge on the rotating f-plane has been subject to several theoretical studies, e.g., Queney (1947), Eliassen and Rekustad (1971), Eliassen and Thorsteinsson (1984), Pierrehumbert (1984), and Pierrehumbert and Wyman (1985). For strictly stationary two-dimensional flow, increased potential temperature on the lee side can result only from condensation heat in precipitation. However, real mountains are not infinite ridges, and the real flow exhibits features that cannot occur in the case of an infinite ridge: the low-level flow is partly or completely diverted around the mountain, with an almost stagnant conditions on the upwind side, and the downslope flow on the lee side may originate from potentially warmer upwind strata above the surface. These features are still imperfectly understood.

Flows past obstacles have been classified by Eliassen (1980), assuming that the lowest isentropic surface coincides with the bottom boundary in the far upstream region. The flows are classified according to (i) whether the obstacle is "isentropic" or "warm", and (ii) non-occurrence or occurrence of closed streamlines. These two classifications form four categories altogether. Several authors have studied the question of occurrence of closed streamlines in the case of a small Rossby number; references are given in Eliassen (1980) and Hogg (1980). Flow at Rossby number of order one has been studied by means of numerical and analytical models based on linearized equations (Vergeiner, 1978; Somieski,

[1] Present affiliation: Icelandic Meteorological Office, Bustadar regur 9, IS-150 Reykjavik, Iceland.

1981; Smith, 1982). The condition for occurrence of a warm obstacle has been considered by Eliassen (1980) for the case of an incompressible fluid without a mean current, and by Smith (1980) from linearized hydrostatic equations in the case of no rotation. The condition given by Smith is in fair agreement with the results in the present paper.

Deflection of air trajectories around a mountain suggests that linear results are unreliable. However, large amplitude effects have not been incorporated into simple three-dimensional continuously stratified models, which describe the way air flows over and around a mesoscale mountain.

This paper describes a three-dimensional isentrope coordinate model that is an extension of the two-dimensional model by Eliassen and Thorsteinsson (1984, hereafter ET). The ET-model is in turn based on the two-dimensional model by Eliassen and Rekustad (1971). The three-dimensional model is capable of predicting some 3-D non-linear features of observed phenomena. A wide range of flow experiments were run, wherein warm obstacles are found in some of the calculations, but closed streamlines do not show up. Thus "isentropic-open" and "warm-open" categories are exhibited in this paper. It is suggested that the collapse of isentropic layers leading to the "warm mountain" case is the mechanism usually responsible for the foehn phenomenon. This foehn theory is different from the classical foehn theories, summarized for example by Atkinson (1981). The model quantifies the magnitudes (in degrees) and downstream extent of the region of foehn warming.

2. Model formulation

2.1. The equations in θ-coordinates

Motion is considered relative to a coordinate frame x, y, θ, which rotates in the absolute sense around the vertical axis with a constant angular velocity $f/2$. Notations used in the following are listed in the Appendix. The dry-adiabatic, hydrostatic, primitive equations in this θ coordinate system read

$$u_t = -\left(\frac{u^2+v^2}{2}\right)_x + vZ - m_x + \kappa(\nabla\cdot\boldsymbol{v})_x - \mu(u-U), \tag{2.1}$$

$$v_t = -\left(\frac{u^2+v^2}{2}\right)_y - uZ - m_y + \kappa(\nabla\cdot\boldsymbol{v})_y - \mu v, \tag{2.2}$$

$$p_{t\theta} = -(up_\theta)_x - (vp_\theta)_y, \tag{2.3}$$

$$m_\theta = \Pi, \tag{2.4}$$

where

$$Z = f + v_x - u_y = f + \xi, \quad m = gz + \Pi\theta$$
$$\text{and } \Pi = c_p\left(\frac{p}{10^5\ \text{Pa}}\right)^{R/c_p}. \tag{2.5}$$

The next to the last term on the r.h.s. of eqs. (2.1) and (2.2) was proposed by Sadourny (1975). This term represents a small linear horizontal diffusivity on the horizontal divergence. This conservative force (curl $\nabla(\kappa\nabla\cdot\boldsymbol{v}) = 0$) is included for numerical purposes. It provides a damping, which by acting selectively on the divergent part of the motion, affects the general vorticity distribution only slightly. The coefficient μ is commented on in Sections 3 and 5.1. The form of the primitive equations (2.1)–(2.4) (without the Rayleigh friction term) is used to develop potential vorticity and enstrophy conserving schemes. A derivation of this equation form (including diabatic but excluding diffusive contributions) has been outlined by Bleck (1979) in a hybrid coordinate frame.

With no Rayleigh friction the equations (2.1)–(2.3) yield the following form of prognostic equation for the potential vorticity, q,

$$q_t + uq_x + vq_y = 0, \tag{2.6}$$

where

$$q = -\frac{Z}{(p_\theta)}. \tag{2.7}$$

The atmosphere is bounded at top and bottom by constant potential temperature surfaces $\theta = \theta_T$ and $\theta = \theta_G$, respectively. Orography is introduced through the lower boundary condition of the form

$$m(x, y, \theta_G, t) = \theta_G \Pi(x, y, \theta_G, t) + g\alpha(t)\, h_m h\left(\frac{x}{L}, \frac{y}{L}\right) - fUy \quad \text{at } \theta = \theta_G. \tag{2.8}$$

Here, $h(\xi, \eta)$ gives the mountain profile, L its half-width, and h_m the crest-height (assumed to be located at $x, y = 0, 0$ with $h(0, 0) = 1$). The factor $\alpha(t)$ is defined to be zero initially and to grow gently to unity during some finite time interval.

The upper boundary condition on $\theta = \theta_T$ is taken to be a free surface with constant pressure; thus

$$p(x, y, \theta_T, t) = p_T \quad \text{or} \quad m_\theta(x, y, \theta_T, t) = \Pi(p_T). \tag{2.9}$$

To avoid reflection of vertically-propagating wave energy from the upper boundary, Rayleigh friction is applied in the upper part of the vertical domain.

The formulas for the geostrophic wind components are

$$u_g = -\frac{1}{f}\frac{\partial m}{\partial y}, \tag{2.10a}$$

$$v_g = \frac{1}{f}\frac{\partial m}{\partial x}. \tag{2.10b}$$

2.2. Partition of dependent variable

The large-scale current is a known, steady, uniform geostrophic flow aligned along the x-direction. The Montgomery potential may then be partitioned into two parts: one, m_1, which balances the large-scale wind, and another, m_2, representing the hydrostatic variation of the Montgomery potential at θ surfaces. This partitioning is formally given by

$$m = m_1(y) + m_2(x, y, \theta, t). \tag{2.11}$$

We substitute this expression into eqs. (2.1), (2.2) and (2.4) and find

$$u_t = -\left(\frac{u^2+v^2}{2}\right)_x + vZ - m_{2x} + \kappa(\nabla\cdot \boldsymbol{v})_x - \mu(u-U), \tag{2.12}$$

$$v_t = -\left(\frac{u^2+v^2}{2}\right)_y - (uZ + m_{1y}) - m_{2y} + \kappa(\nabla\cdot \boldsymbol{v})_y - \mu v, \tag{2.13}$$

$$m_{2\theta} = \Pi. \tag{2.14}$$

We start from the large-scale flow field. It consists of rectilinear barotropic flow along the x-axis in geostrophic and hydrostatic equilibrium; thus m_1 and the initial Montgomery potential $M_2(\theta)$ satisfy

$$m_{1y} = M_{1y} = -fU, \quad M_{2\theta} = \Pi(P), \tag{2.15a, b}$$

respectively. Here U and $P(\theta)$ are the large-scale flow and large-scale pressure distribution, respectively. M_2 and P must satisfy the boundary conditions (2.8) and (2.9), with $\alpha(0) = 0$.

To complete the definition of the large-scale flow, we must also define the mass distribution. The relation between $\Pi(P)_\theta$ and N^2 may be shown to be

$$\Pi(P)_\theta = -g^2 N^{-2} \theta^{-2}. \tag{2.16}$$

We shall assume the buoyancy frequency N to be constant initially everywhere in the atmosphere. Then from (2.16)

$$\Pi(P) = \Pi(p_T) + \frac{g^2}{N^2}\left(\frac{1}{\theta} - \frac{1}{\theta_T}\right), \tag{2.17}$$

and from (2.15b)

$$M_2(\theta) = \Pi(p_T)\theta + \frac{g^2}{N^2}\left(\frac{\theta_T - \theta}{\theta_T} + \ln\frac{\theta}{\theta_G}\right). \tag{2.18}$$

These equations, applied for all values of x, y, complete the definition of the initial state.

The initial pressure and velocity are uniform on each isentropic surface, so the potential vorticity is equal to $Q = f/(-P_\theta)$. Eq. (2.6) may then be integrated to

$$q(x, y, \theta, t) = Q(\theta) \quad \text{or} \quad \frac{f + v_x - u_y}{(-p_\theta)} = \frac{f}{(-P_\theta)}. \tag{2.19a, b}$$

Initially, the slope of the isobaric surfaces is in geostrophic balance with the zonal flow. The assumption of a barotropic initial state implies that the isentropic surfaces coincide with the isobaric surfaces. Specification of a non-uniform potential temperature on a level sea surface makes the lower boundary condition cumbersome to code. That difficulty is avoided by assuming θ uniform on the lower boundary. This condition yields a nearly horizontal rigid bottom plane, $z = -fUg^{-1}y$. Hereafter, this plane will be referred to as a reference bottom plane, since z no longer equals zero at the lower boundary. As long as the reference bottom plane deviates only slightly from the horizontal this is assumed to be of little consequence for our analysis.

On the reference bottom plane, a mountain is progressively built up during the first stages of the integration, to its final height above this plane. The centre of the mountain is at the origin of the coordinate system (see Fig. 1). Since the reference ground is an isentropic surface, the condition placed on the time-dependent deviation, ζ, relative to the reference bottom plane can be expressed as

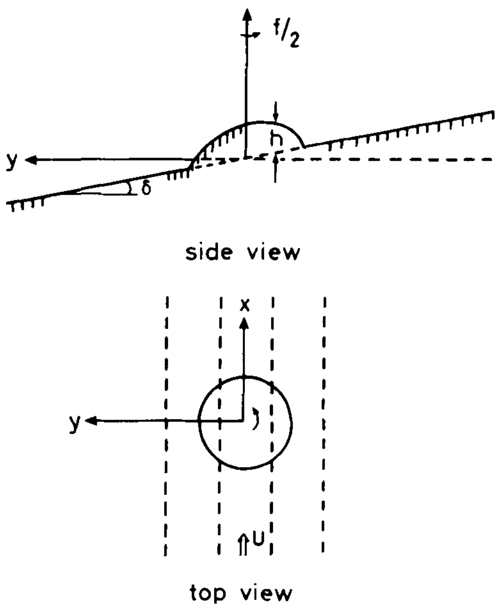

Fig. 1. Perspective views of the three-dimensional problem from side and top. The system is assumed to be rotating about the vertical axis with constant angular velocity $f/2$. The isolated topography is on a sloping plane ($z_y = \tan\delta$, $\tan\delta \ll 1$); the mountain grows during the integration. Dashed lines denote lines of equal depth of the reference bottom plane. The geostrophically balanced flow U is modified by the properties of the mountain.

$$\zeta(x, y, \theta_G, t) = z(x, y, \theta_G, t) - (-z_y y) = g^{-1}(m_2 - \theta m_{2\theta})_{\theta=\theta_G} = \alpha(t)\, h_m h\left(\frac{x}{L}, \frac{y}{L}\right), \tag{2.20}$$

where $\alpha(t)$ increases from $\alpha(0) = 0$ to $\alpha(t) = 1$ when $t \geqslant t_0$. In the modified system of equations, eq. (2.8) is replaced by the condition

$$m_2(x, y, \theta_G, t) = \theta_G \Pi(x, y, \theta_G, t) + g\alpha(t)\, h_m h\left(\frac{x}{L}, \frac{y}{L}\right). \tag{2.21}$$

Consider a hypothetical air particle moving with the geostrophic wind. In a stationary situation the geostrophic stream function $\eta_g(x, y)$ in a surface of constant potential temperature must satisfy

$$\eta_g = \frac{m_2 - fUy}{fU}. \tag{2.22}$$

If the motion is conservative and the waves steady, the real streamline $\eta(x, y)$ may be obtained from the Bernoulli function

$$\tfrac{1}{2}(u^2 + v^2) + m_2 - fUy - \kappa\nabla\cdot\mathbf{v} = B, \tag{2.23}$$

with B constant along each streamline.

The location of a selected isentropic surface in the xz-plane may be obtained from

$$g\zeta(x, y, \theta) = m_2 - \theta m_{2\theta}. \tag{2.24}$$

3. The numerical model

As in ET, the mass continuity equation (2.3) is replaced by the integrated potential vorticity equation (2.19b). Thus our model comprises eqs. (2.12)–(2.14) and (2.19b). Applying constant potential temperature along the top and bottom of the model atmosphere provides both barotropic and baroclinic stability of our uniform basic current to wave disturbance (Charney and Stern, 1962).

The finite difference scheme is based on a four dimensional, rectangular grid ($i\Delta x$, $j\Delta y$, $\theta_G + k\Delta\theta$, $n\Delta t$) in the $xy\theta t$-space. The vertical arrangement of the dependent variables is shown in Fig. 2 and the horizontal arrangement in Fig. 3. This "Eliassen" type time- and space-staggered grid provides fast computations, and minimizes the truncation errors for the potential vorticity

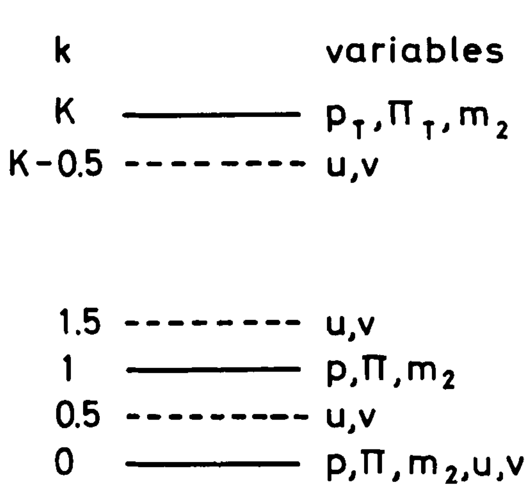

Fig. 2. Vertical distribution of variables with K vertical layers.

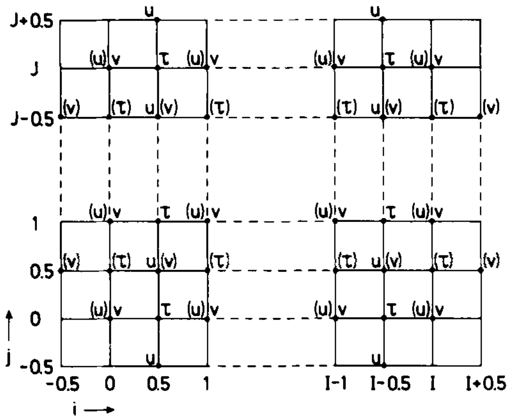

Fig. 3. Horizontal distribution of variables at integer and half-integer steps. The variables defined at half-integer time steps are in parentheses. τ denotes any of the variables ξ, Z, p, Π, m_2.

equation (2.19b). The finite difference analogues of equations (2.12) and (2.13) are first used to calculate tentative new values $u_*^{n+1/2}$ and $v_*^{n+1/2}$:

$$u_*^{n+1/2} = u^{n-1/2} - \left(\delta_x \frac{\overline{u^2}^y + \overline{v^2}^x}{2} - v\delta_\theta \bar{p}^x Q + \delta_x \overline{m_2}^\theta\right)^n - \mu(u-U)^{n-1/2}, \quad (3.1)$$

$$v_*^{n+1/2} = v^{n-1/2} - \left(\delta_y \frac{\overline{u^2}^y + \overline{v^2}^x}{2} + (u\delta_\theta \bar{p}^y Q - U\Delta_\theta PQ) + \delta_y \overline{m_2}^\theta\right)^n - \mu v^{n-1/2}. \quad (3.2)$$

The accepted new values are then computed from

$$u^{n+1/2} = u_*^{n+1/2} + \kappa \tfrac{1}{2}\delta_x((\nabla\cdot \boldsymbol{v}_*)^{n+1/2} + (\nabla\cdot \boldsymbol{v})^{n-1/2}), \quad (3.3a)$$

$$v^{n+1/2} = v_*^{n+1/2} + \kappa \tfrac{1}{2}\delta_y((\nabla\cdot \boldsymbol{v}_*)^{n+1/2} + (\nabla\cdot \boldsymbol{v})^{n-1/2}). \quad (3.3b)$$

The finite difference analogues of equations (2.19b) and (2.14) are

$$\delta_\theta p = (f + \delta_x v - \delta_y u)/Q, \quad (3.4)$$

$$\delta_\theta m_2 = \overline{\Pi}^\theta. \quad (3.5)$$

The symbols δ and $\overline{(\ )}$ are the centred difference and average operations over one grid mesh. The superscript n is the time index. The coefficient μ is set equal to zero everywhere except near the upper boundary. Consequently, the conservation of potential vorticity is not retained in the upper model layers. This inconsistency is thought to be of little consequence. In the absorbing layer the results have little meaning anyway. The use of the κ divergence damping is required for the finite-amplitude simulations to stabilize non-linear numerical instabilities. This is accomplished by fixing κ at the smallest value sufficient to maintain stability. For the Ro = 1 simulations conducted, the coefficient κ was held so as to damp the divergent waves with wavelengths L and $3L$ to e^{-1} of their original values in approximately 0.11 and 1 hours, respectively. This effect is reduced for longer divergent flow components.

The computations are made on a rectangular grid bounded by two transversal boundaries, $i = 0$ and $i = I$, and two lateral boundaries, $j = 0$ and $j = J$. Here I and J are always integers. Thus, referring to Fig. 3, at the transversal boundaries u and ξ are required for all half-integer steps, and at the lateral boundaries v and ξ are required for all integer steps. A method based on the extrapolation procedure of Orlanski (1976) is used to obtain boundary values of both the velocity components normal to the boundary (i.e., u on the transversal and v on the lateral boundaries) and the relative vertical vorticity at these four open boundaries. In demonstrating the method, the treatment of a boundary point located at array location (i, J) is discussed. There should be no difficulties in writing the numerical formulation for the other three boundaries. Referring to Fig. 4, which shows a configuration of the esti-

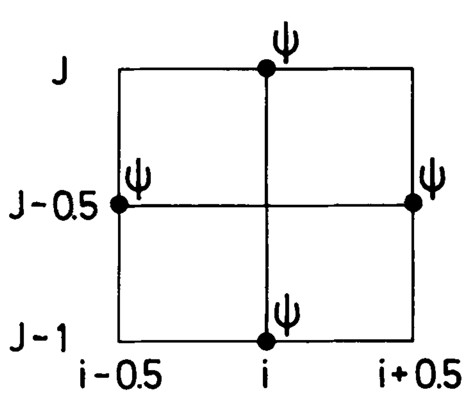

Fig. 4. Configuration close to the $j = J$ boundary of the estimated variable ψ, referred to in eqs. (3.6), (3.7) and (3.8).

mated variable ψ in the xy plane close to the boundary $j = J$, the method may be briefly described as follows: First, the local phase speed associated with ψ is determined from

$$c_\psi = \begin{cases} 0 & \text{if } \beta \leqslant 0 \\ \beta \dfrac{\Delta y}{\Delta t} & \text{if } 0 < \beta < 1 \\ \dfrac{\Delta y}{\Delta t} & \text{if } \beta \geqslant 1, \end{cases}$$

$$\beta = -\frac{\psi^n_{i+1/2,J-1/2} + \psi^n_{i-1/2,J-1/2}}{2(\psi^{n-1/2}_{i,J} - \psi^{n-1/2}_{i,J-1})} - \frac{-\psi^{n-1}_{i+1/2,J-1/2} - \psi^{n-1}_{i-1/2,J-1/2}}{2(\psi^{n-1/2}_{i,J} - \psi^{n-1/2}_{i,J-1})}, \tag{3.6}$$

where n is the time index. Then $\psi^{n+1/2}_{i,J}$, is obtained from

$$\psi^{n+1/2}_{i,J} = \psi^{n-1/2}_{i,J} - c_\psi \frac{\Delta t}{\Delta y} [\psi^{n+1/2}_{i,J} + \psi^{n-1/2}_{i,J} - (\psi^n_{i+1/2,J-1/2} + \psi^n_{i-1/2,J-1/2})]. \tag{3.7}$$

Before applying (3.7), the c_ψ values are smoothed by means of a three-point Shapiro (1970) filter, involving the adjacent points above and below.

Immediately after applying (3.7), the values of normal velocity are subjected to a Newtonian damping, that constrains them to relax back towards the environmental value ψ_0 on a time scale that depends on whether the phase velocity is pointed into or out of the integration area. The damping is of the form

$$\psi = \psi^* + \frac{1}{A}(\psi_0 - \psi^*),$$

$$A = \begin{cases} A_1 & \text{if } \beta \geqslant 0 \\ A_2 & \text{if } \beta < 0, \end{cases} \tag{3.8}$$

where ψ^* and ψ are the dependent variable to be relaxed and the relaxed value, respectively, and A is the damping coefficient (with constant values A_1 and A_2). This is a variation of the time relaxation procedure used by Kurihara and Bender (1983) and others. (This relaxation procedure has little beneficial effect.)

To compute the velocity component tangential to the open boundary on the side boundaries it is necessary to assume values of this velocity component just outside the model boundary for use in the advective terms. Analogous to Ross and Orlanski (1982), the relative vertical vorticity at each point is used directly to obtain the boundary condition for the above variable from definition of vorticity. For the $j = J$ boundary example this is computed as follows:

$$u^{n+1/2}_{i,J+1/2} = u^{n+1/2}_{i,J-1/2} - \Delta y \xi^{n+1/2}_{i,J} + \frac{\Delta y}{\Delta x}(v^{n+1/2}_{i+1/2,J} - v^{n+1/2}_{i-1/2,J}). \tag{3.9}$$

To obtain the boundary values of p, the radiation condition is not used, but instead the potential vorticity eq. (3.4) is applied. The above treatment of the velocity component tangential to and outside of the open boundary, and of pressure at the boundary via the vertical relative vorticity, reduces the values of spurious vorticities (Montgomery potentials) due to boundary errors.

The integration procedure is as follows. When the precise u and v values are known up to time t, $p(t)$ is obtained from (3.4) by vertical integration, starting from the top where p is known from (2.9). Then $m_2(t)$ is obtained from (3.5) by vertical integration starting from the bottom where, according to (2.21), m_2 has the value

$$m_{2G} = \theta_G \Pi(p_G) + \alpha(t) g h_m h\left(\frac{x}{L}, \frac{y}{L}\right). \tag{3.10}$$

The values for $u(t + 1/2\Delta t)$ and $v(t + 1/2\Delta t)$ are then calculated from (3.1), (3.3a), (3.2) and (3.3b). The velocity components at ground level (Fig. 2) are obtained from (3.1), (3.3a), (3.2) and (3.3b) without vertical averaging. Because of the staggering in space and time, the side boundary conditions are only applied on the lateral boundaries at the integer value time steps, and only on the transversal boundaries at the intermediate time steps.

4. Non-dimensional variables

These ideas on how to express the results in non-dimensional form are derived from Pierrehumbert and Wyman (1985). Non-dimensionalization is achieved by scaling x, y by the characteristic mountain half-width L, u and v by a typical velocity U, t by L/U, m_1 and m_2 by fLU, p by p_0 ($= 10^5$ Pa), θ by $\theta^* = U^2/c_p$ and Π by c_p. In these non-dimensional units the initial conditions on pressure (2.17), the system (2.12)–(2.14) and (2.19b) (without the Rayleigh friction term), and the boundary condition at bottom (2.21) are

$$\Pi(P) = (P)^{R/c_p} = \Pi_T + \frac{1}{S}\left(\frac{1}{\theta} - \frac{1}{\theta_T}\right), \tag{4.1}$$

$$\mathrm{Ro}\, u_t = -\mathrm{Ro}\left(\frac{u^2 + v^2}{2}\right)_x + vZ - m_{2x} + \kappa'(\nabla \cdot \boldsymbol{v})_x, \tag{4.2}$$

$$\mathrm{Ro}\, v_t = -\mathrm{Ro}\left(\frac{u^2 + v^2}{2}\right)_y - (uZ + m_{1y}) - m_{2y} + \kappa'(\nabla \cdot \boldsymbol{v})_y, \tag{4.3}$$

$$m_{2\theta} = \mathrm{Ro}\, \Pi, \tag{4.4}$$

$$\frac{\partial p}{\partial \theta} = \left(1 + \mathrm{Ro}\frac{\partial v}{\partial x} - \mathrm{Ro}\frac{\partial u}{\partial y}\right)\frac{c_p}{R}\frac{1}{S}\frac{P^{c_v/c_p}}{\theta^2}, \tag{4.5}$$

$$m - \theta m_\theta = \alpha\sigma h \quad \text{if}\ \frac{1}{\theta} = \frac{1}{\theta_G} = \frac{1}{\theta_T} + S(\Pi_G - \Pi_T). \tag{4.6}$$

Here we operate with

$$\mathrm{Ro} = \frac{U}{fL}, \tag{4.7}$$

$$S = (NU/g)^2, \tag{4.8}$$

$$\sigma = \frac{gh_m}{fLU} = \frac{H}{S^{1/2}}\mathrm{Ro}, \tag{4.9}$$

in which $H = Nh_m/U$. With the particular scaling used in the experiments, it can be deduced that

$$\kappa' = \frac{\kappa}{fL^2}. \tag{4.10}$$

The non-dimensional parameters appearing in the non-dimensional equations (4.1)–(4.6) are Ro, S, H and κ'. The non-dimensional parameter κ' appears because of numerical reasons. Its effects on the large amplitude divergent flow are assumed negligible. Therefore, κ' is omitted and it is assumed that this idealized non-linear flow problem is completely controlled by the three non-dimensional numbers, Ro, S and H. Note that of these three numbers only Ro is dependent on f. This occurs in a product of fL. Therefore, for similar flows the effect of changing f is equivalent to an inverse proportional change in L. In this paper N and U are kept constant and the number S has a constant value. Thus, in the experiments only the two non-dimensional parameters Ro and H are varied. The character of the flow as a function of these two parameters was investigated. The primary interest is in how large the anomalous potential temperature becomes immediately downstream of the mountain, as this characterizes the strength of the foehn effect produced by the mountain.

All results are presented in terms of the above non-dimensional units.

5. Description and comparison of solutions

5.1. *Experimental design*

The results of five theoretical examples (experiments 1–5), performed with the described three-dimensional model, are presented below. In all these experiments, the three-dimensional orography is represented as

$$h\left(\frac{x}{L}, \frac{y}{L}\right) = \begin{cases} \frac{1}{2}\left(1 + \cos\left(\frac{\pi}{2L}\sqrt{x^2 + y^2}\right)\right) & \text{if } \sqrt{x^2 + y^2} < 2L \\ 0 & \text{if } \sqrt{x^2 + y^2} \geqslant 2L. \end{cases} \tag{5.1}$$

The horizontal domain lies between $-5.6L \leqslant x, y \leqslant 5.6L$. The horizontal grid increments Δx and Δy are held fixed at $0.4L$ for all runs. The two-dimensional xz-plane located at $y = 0$ is referred to as the central xz-plane. The mountain grows from zero to full size in $Ut/L = 5.6085$. The atmosphere is divided vertically into 17 levels with potential temperatures of

$$\theta_k = (275 + 3.0 \times k)\,°\mathrm{K}/\theta^*, \qquad k = 0, 1, \ldots, 8,$$
$$\theta_k = (299 + 4.3 \times (k - 8))\,°\mathrm{K}/\theta^*, \quad k = 9, \ldots, 16,$$

where θ^* is the unit of potential temperature. The Rayleigh friction coefficient is taken to be a function of k:

$$\mu_k = \begin{cases} \mu_T \sin^2\left(\frac{\pi}{2}\frac{\ln(\theta_k/\theta_8)}{\ln(\theta_T/\theta_8)}\right), & k > 8 \\ 0, & k \leqslant 8. \end{cases} \tag{5.2}$$

The following non-dimensional values are used:

$$p_G = 1, \qquad \frac{U}{L}\Delta t = 0.0104,$$

$$\frac{\kappa}{fL^2} = \frac{6}{1.3} \cdot 10^{-1}, \quad \frac{\mu_T}{f} = 1,$$

$$A_1/f = 10^{12}, \qquad A_2/f = 10^9.$$

Table 1. *Parameter values used in the experiments*

Experiment	L (km)	h_m (km)	Ro	H
1	100	1.0	1.0	1.0
2	100	2.5	1.0	2.5
3	250	2.5	0.4	2.5
4	25	1.0	4.0	1.0
5	250	4.0	0.4	4.0

The fixed dimensional values in the non-dimensional numbers are: $U = 13$ m s^{-1}, $N = 100f = 1.3 \times 10^{-2}$ s^{-1} and $g = 9.81$ m s^{-2}. These values are used to produce data (in the manner described in Sections 2 and 3) for five situations, i.e., experiments 1–5. These only differ with regard to mountain height and mountain half-width. Integrations are made for the 5 combinations of Ro and H shown in Table 1, which also give half-width and height of the mountain in each case. Other flows with the same Ro, S and H could have been chosen. This experimental design permits the following systematic comparisons of flow behaviour:

(i) effect of variation of H, other non-dimensional numbers being fixed.
(ii) effect of variation of Ro, other non-dimensional numbers being fixed.

Experiment 5 was performed to investigate a large amplitude case, but figures from this experiment are not shown because of space limitations.

5.2. *Mass flux*

In the steady state, consider a stream tube confined between the isentropic surfaces θ and $\theta + \Delta\theta$, and let the tube far upstream be bounded by the vertical planes Y and $Y + \delta Y$. Since the tube carries the same mass flux through any of its cross-sections, we have

$$u\,\delta p\,\delta y = U\,\delta P\,\delta Y, \tag{5.3}$$

where δy is the width of the tube and δp the pressure difference between the two θ-surfaces at an arbitrary cross-section. It follows that

$$\gamma = \frac{\delta Y}{\delta y} = \frac{u\,\delta p}{U\,\delta P} \tag{5.4}$$

is a measure of the widening of the stream tube. Here we present results of flow across mountains which may be easily understood by these constant mass flux properties.

5.3. *Time to reach a steady state*

The time it takes to evolve the steady state characteristics of gravity–inertia waves can be understood in terms of energy propagation ideas. These waves are composed of essentially vertical and downstream propagating wave components. In the two-dimensional case of constant U and N, the rays are straight lines sloping upward in the downstream direction, and the steepness decreases with increasing horizontal wavelength. Linear analysis by Queney (1973) shows that in this case wave energy is transmitted with group velocity reaching its maximum value U in the horizontal direction (its minimum value, of the order of $\frac{1}{10}U$, is in the vicinity of the vertical direction).

The lower boundary reaches its full height after a non-dimensional integration time $(U/L)t = 5.6085$. The differences between the results at non-dimensional times $(U/L)t = 7.478$ and 9.36 are very slight throughout the integration area. We can thus assume that the motion within the integration area is in a quasi-stationary equilibrium. This assumption is roughly consistent with the group velocity concept introduced previously, as mountain amplitude changes relatively little after $(U/L)t = 3.0$ and it takes a particle $(U/L)t = 5.6$ units to cross the downstream domain. Only results for $(U/L)t = 9.36$ are shown.

5.4. *Computed flow fields*

In all six runs the three-dimensional perturbations produced in the air flow were seen to consist of (1) upward propagating hydrostatic gravity–inertia waves located immediately above and to the lee of the mountain, and (2) low level flow splitting around the mountain accompanied by the descent of potentially warmer air over and on the downstream side of the mountain.

Experiment 1 (Ro = 1.0 and $H = 1.0$) (see Fig. 5). The cross-section of the isentropic surfaces in the central vertical plane $y = 0$ (Fig. 5a) shows wave features similar to those appearing in the calculations for an infinite ridge: a gravity–inertia wave over the mountain and on the lee side, with phase lines tilted towards the windward side, indicating an upward wave energy flux. The thickness of the lowest isentropic layer is seen to be slightly increased on the upwind side of the mountain and also at some distance on the lee side. However, over the mountain peak and particularly at the lee slope, the thickness is strongly reduced. This also holds for the pressure thickness Δp.

Fig. 5b shows the contours of the non-dimensional vorticity $10\xi/f$ (solid lines) at the surface $\theta_{0.5}$ in xy-projection. A region of strong anticyclonic vorticity centred over the lee mountain slope is surrounded by a region of weaker cyclonic vorticity. According to the potential vorticity theorem, the pressure thickness Δp of an

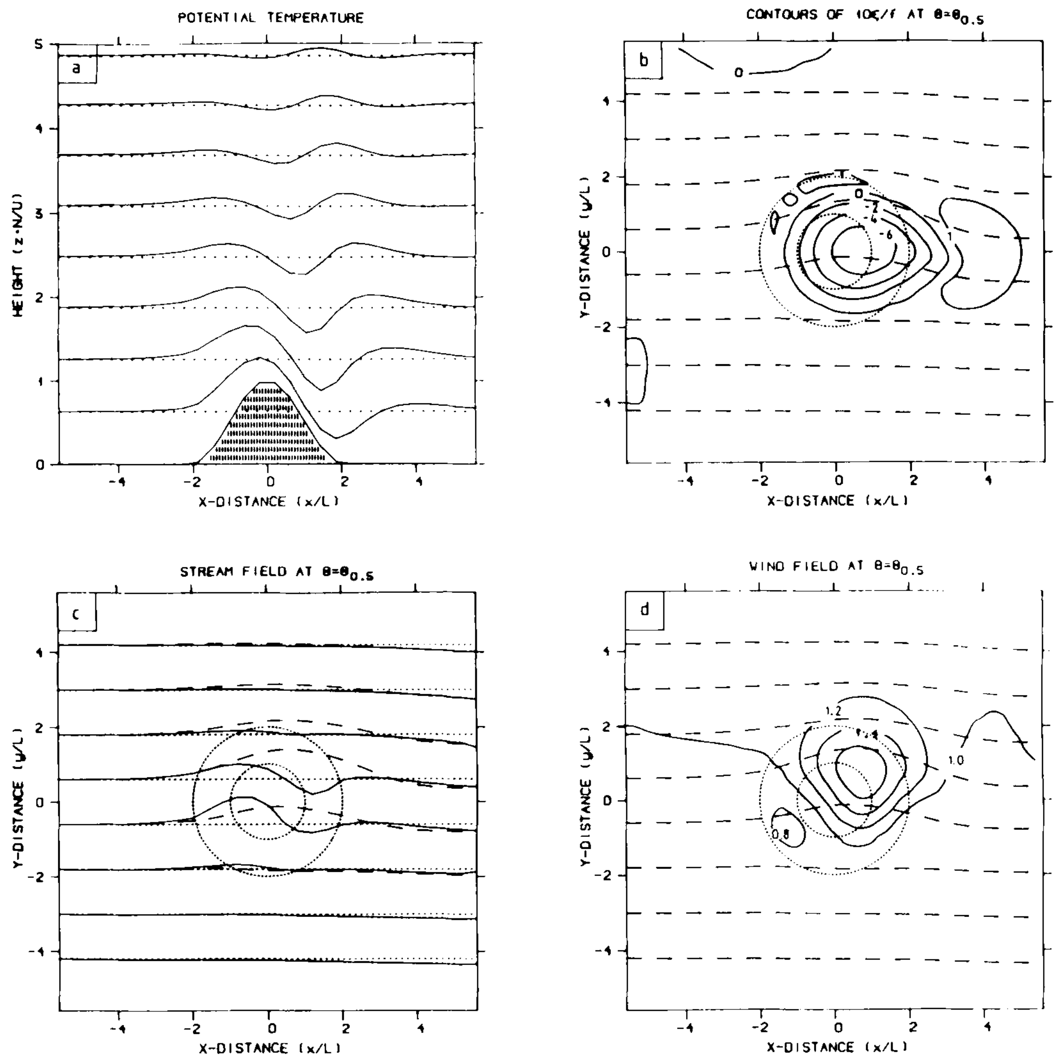

Fig. 5. Experiment 1. Results for flow past an isolated circular mountain (eq. 5.1) with $H = 1.0$ and $\mathrm{Ro} = 1.0$. The two concentric dotted circles in the plan view indicate radiuses of L and $2L$, respectively, of the orography profile. (a) The center plane $y = 0$ showing the intersection curves with the isentropic surfaces $k = 0, 1, \ldots, 8$ (heavy lines). (b) xy-projection of air trajectories $\eta(x, y)$ (dashed curves) and contours of $10\xi/f$ (solid) in the $\theta_{0.5}$ surface. (c) xy-projection of air trajectories $\eta(x, y)$ (dashed curves) and geostrophic trajectories η_g (solid) in the $\theta_{0.5}$ surface. (d) xy-projection of air trajectories $\eta(x, y)$ (dashed curves) and contours of absolute value of velocity (solid) in the $\theta_{0.5}$ surface.

isentropic layer varies in proportion to its absolute vorticity $f+\xi$; therefore the contours may also be interpreted as representing constant values of $10(\Delta p/\Delta P - 1)$. The pattern is seen to be in agreement with the variations of Δp of the lowest layer, which is evident from Fig. 5a.

Fig. 5c shows the streamlines (dashed curves) and geostrophic stream function η_g (solid curves) at the surface $\theta_{0.5}$ in xy-projection. They are calculated from (2.23) and (2.22), respectively. The η_g-lines show a ridge centred over the windward mountain slope and a trough over the lee slope. The streamlines approaching the mountain bend to the left, curving anticyclonically over and to the left of the lee slope. Vorticity due to streamline curvature is in rough agreement with the vorticity distribution in Fig. 5b. There is a crowding of streamlines on the left side of the mountain.

The isotachs (non-dimensional) in the middle of the lowest layer are shown in Fig. 5d. A wind maximum of more than 1.6 and a wind minimum of about 0.8 form a dipole pattern centred over the mountain peak with the axis at 45° relative to the x-axis.

Experiment 2 (Ro = 1.0 and $H = 2.5$). The cross-section shown in Fig. 6a shows a wave pattern similar to that of experiment 1 (Fig. 5a), but with a little larger amplitude. It does not exhibit θ-surface overturning. The wave pattern differs qualitatively from that of experiment 1 in that the three lowermost isentropic layers have collapsed over the lee slope, i.e., their thickness is virtually zero. On the upper part of the lee slope, the fourth layer reaches the ground as a warm foehn wind. This potentially warmer air comes from a nearly 2 km height upstream ($\theta = \theta_3$ level). At approximately $x = 3L$ the potentially warmer air is again lifted above the colder air (entering around the mountain from the left side).

The absolute vorticity vanishes in the collapse region. Fig. 6b shows the relative vorticity in the middle of the lowest isentropic layer. The collapse region where $\xi = -f$ extends from the uppermost windward slope, over the lee slope and to part of the lee side plain. Corresponding ξ contours for the next two isentropic layers (the first one being shown in Fig. 6e) indicate smaller collapse regions confined to the lee slope.

The η_g-field in the $\theta_{0.5}$ surface (Fig. 6c) is strongly disturbed over a large region, showing a very strong trough on the lee slope and a closed high on the upwind side. Compared with Fig. 5c ($H = 1$), the windward ridge and the lee trough are strongly enhanced. Notice that these fields have no meaning within the collapse region, where they should be replaced by fields at higher θ-values.

While the low level air flow in the $H = 1.0$ calculation (Fig. 5c) is partly deflected to the left as it approaches the mountain (Northern Hemisphere), in the $H = 2.5$ calculation most of the low-level air (Fig. 6c) flows around the mountain on the left side and only a very small proportion goes over the mountain. The streamlines of Fig. 6c reveal that the cold air from the lowest model layer noted downstream of $x = 3L$ in Fig. 6a has been deflected around the mountain and stems from the lowest isentropic layer upstream. This low-level air, which has been diverted around the mountain on both sides, bends back and comes together on the lee side, forcing potentially warmer air up above the surface (cf. Fig. 6a). This process determines the downstream extent of the warm collapse region.

Comparing the wind field in Fig. 6d ($H = 2.5$) and Fig. 5d ($H = 1.0$) we find that the location of maximum and minimum wind speed is little affected by this change in H, but the changes of the perturbation amplitude of the wind speed are nearly linear. The region of increased wind speed extends somewhat further outward from the mountain near the ground than in the $H = 1.0$ case. This is consistent with the downward deflection of potential temperature surfaces. Again, however, the collapse region should be excepted. Wind field at ground level (not shown) shows that almost stagnant conditions exist on the upwind side.

The leftward deflection of streamlines decreases rapidly with height (Figs. 6b, e, g). The air parcels in the second (Fig. 6e) and third (Fig. 6g) lowest layer are deflected around the mountain, and reach the ground on the lower part of the lee slope and on part of the lee side plain (Figs. 6a, b, f, g).

Meso scale potential temperature features are displayed in the field $(\theta_{\text{surface}} - \theta_G)/\theta^*$, where θ_{surface} denotes the potential temperature of the highest isentropic surface in contact with the ground. This potential temperature difference field permits separation of the meso anomalies from the background potential temperature structure. Fig. 6f shows the contours of $(\theta_{\text{surface}} - \theta_G)/\theta^*$ at contour intervals of $3012/169 \approx 18$ at ground surface. The three contours in this figure correspond to the collapse region $\xi = -f$ for each of the three lowest isentropic layers. For $\theta^* = 1/6$ these contours correspond to 3, 6 and 9°K, respectively. The maximum of the potential temperature anomalies is close to 54 and is located at the upper lee side plain. From Figs. 6b, e, g it is seen that the maximum of $(\theta_{\text{surface}} - \theta_G)/\theta^*$ is connected with the strongest splitting of the flow.

At the level $\theta = \theta_{2.5}$, the flow splitting is not as pronounced, and the left–right asymmetry of streamlines around the mountain is decreased. The velocity field at $\theta = \theta_{2.5}$ reveals that the leftward jet and region of reduced wind velocity are shallow.

Concerning sensitivity of the flow response to the κ divergence damping: an equivalent 2-D numerical model experiment with the same κ damping and Ro = 1.0 (not shown here) exhibits near wave overturning for $H = 1.75$, and breakdown of the calculation happens at $H = 2.0$. Wave overturning occurs at a higher value for H in the 3-D case, because the vertical motion is decreased by the three-dimensional nonlinearities of the flow. Presumably wave overturning in this 3-D case (Ro = 1.0 and $H = 2.5$) is inhibited by a 3-D flow, not by the κ damping. More serious is that the κ divergence damping may reduce the maximum horizontal divergence at the lee slope and consequently the collapse of θ-surfaces.

Experiment 3 (Ro = 0.4 and $H = 2.5$). Figs. 7(a)–(d) display a solution for this case. Strongly decelerated flow exists where the wind blows towards higher Montgomery potential on the windward right side. The max/min wind structure exhibits a dipole pattern centred over the mountain peak with the dipole axis at almost 90° relative to the x-axis, i.e., a larger angle than in the Ro = 1.0 cases. The local jet on the left flank is rotated, and the lee wind decreases as a result of the change in Ro as compared with experiment 2. A comparison of Figs. 6 and 7 shows that for Ro = 0.4 a greater proportion of the flow goes over the obstacle, as is consistent with a decreased h_m/L ratio. The horizontal perturbation caused by the Ro = 0.4 case is more symmetric about the y-axis (i.e., windward versus leeward side) than in the Ro = 1 case.

Experiment 4 (Ro = 4.0 and $H = 1.0$). The solution for this case is shown in Figs. 8(a)–(d). The results are quite similar to those for experiment 1. There is near collapse of the lowest isentropic layer. If the lowermost layer had been divided into several layers it is likely that some of them would have collapsed. The reduced pressure thickness of the lowest model layer extends further downstream than in experiment 1 (Ro = 1.0 case). The η_g-field shows greater disturbance, and the flow is more symmetric about the x-axis than in the Ro = 1.0 case. The max/min velocity structure exhibits a dipole pattern centred over the mountain peak with the dipole axis at a smaller angle relative to the x-axis than in the Ro = 1 case (Fig. 5d). This smaller angle is to be expected for this higher Rossby number flow.

Experiment 5 (Ro = 0.4 and $H = 4.0$). The figures from this experiment are not shown here. The collapse of θ-surfaces extends between the locations $x \approx -L$ and $x \approx 2.2L$. Compared with Fig. 7c ($H = 2.5$), the lee trough and especially windward ridge are strongly enhanced. As compared to experiment 3, the location of maximum and minimum wind speed is little affected by this change in H. A wind maximum of more than 3.6 and a wind minimum of almost zero exist in the middle of the lowest layer.

These examples suggest the following conclusions. For Ro $\gg$ 1 one must assume that the earth's rotation has little effect and the low-level flow is nearly symmetric with respect to the central streamline. With decreasing Ro, the low-level flow shows increased asymmetry, and for not too small a value for H, most of the low-level flow passes on the left side of the mountain (Northern Hemisphere). The location of the minimum and maximum wind speeds is most sensitive to the value of Ro, and their strength is most sensitive to H.

5.5. The collapse of θ-surfaces

This subsection concerns effects of variations of Ro and H on the high potential temperature anomaly produced by mountains at ground surface. In all cases the results show that the maximum magnitude (in degrees) of the collapse of θ-surfaces occurs at the upper part of the lee

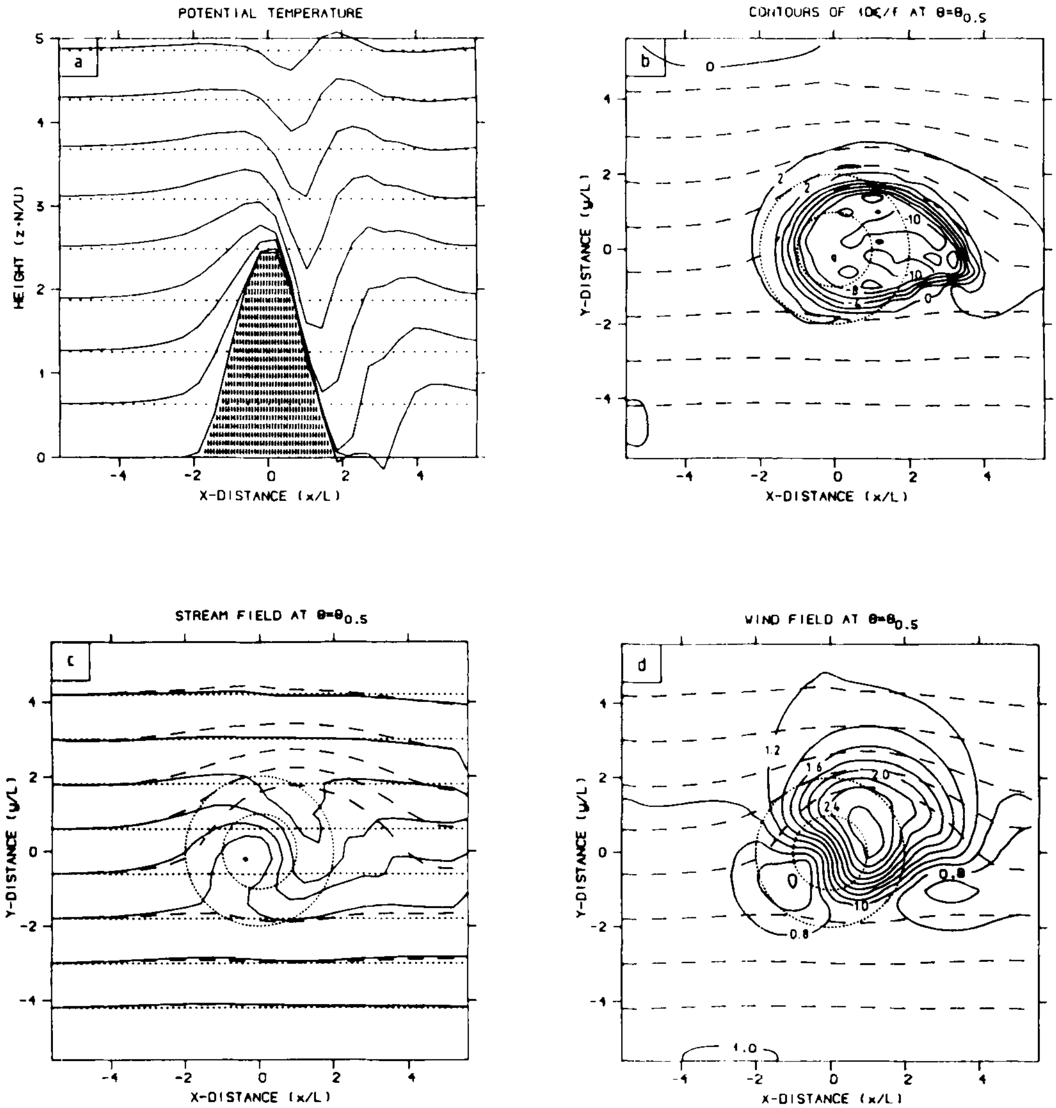

Fig. 6. Experiment 2. Results for flow past an isolated circular mountain (eq. (5.1)) with $H = 2.5$ and $\mathrm{Ro} = 1.0$. Explanation: (a)–(d) as in Fig. 5. (e) as for (b) except level $\theta = \theta_{1.5}$. (f) Contours of $(\theta_{\text{surface}} - \theta_G)/\theta^*$ at contour intervals of 18 at ground surface. (g) as for (c) except level $\theta = \theta_{2.5}$. (h) as for (d) except level $\theta = \theta_{2.5}$.

slope, which is connected with the strongest splitting of the flow at this location.

The two most important characteristics of the pattern of θ-surface collapse are the magnitude (in degrees) and downstream extent of the collapse of θ-surfaces. The former can be conveniently summarized by examining the maximum value of $(\theta_{\text{surface}} - \theta_G)/\theta^*$ (denoted by ϑ) appearing anywhere on the upper lee slope of the mountain. θ_{surface} is subjectively evaluated at the ground surface. With this inaccuracy in mind, we may examine the values of ϑ obtained from the numerical calculations. Fig. 9 gives values of $\mathrm{Ro} = 0.4$, 1.0 and 4.0 in the (H, ϑ) plane. For

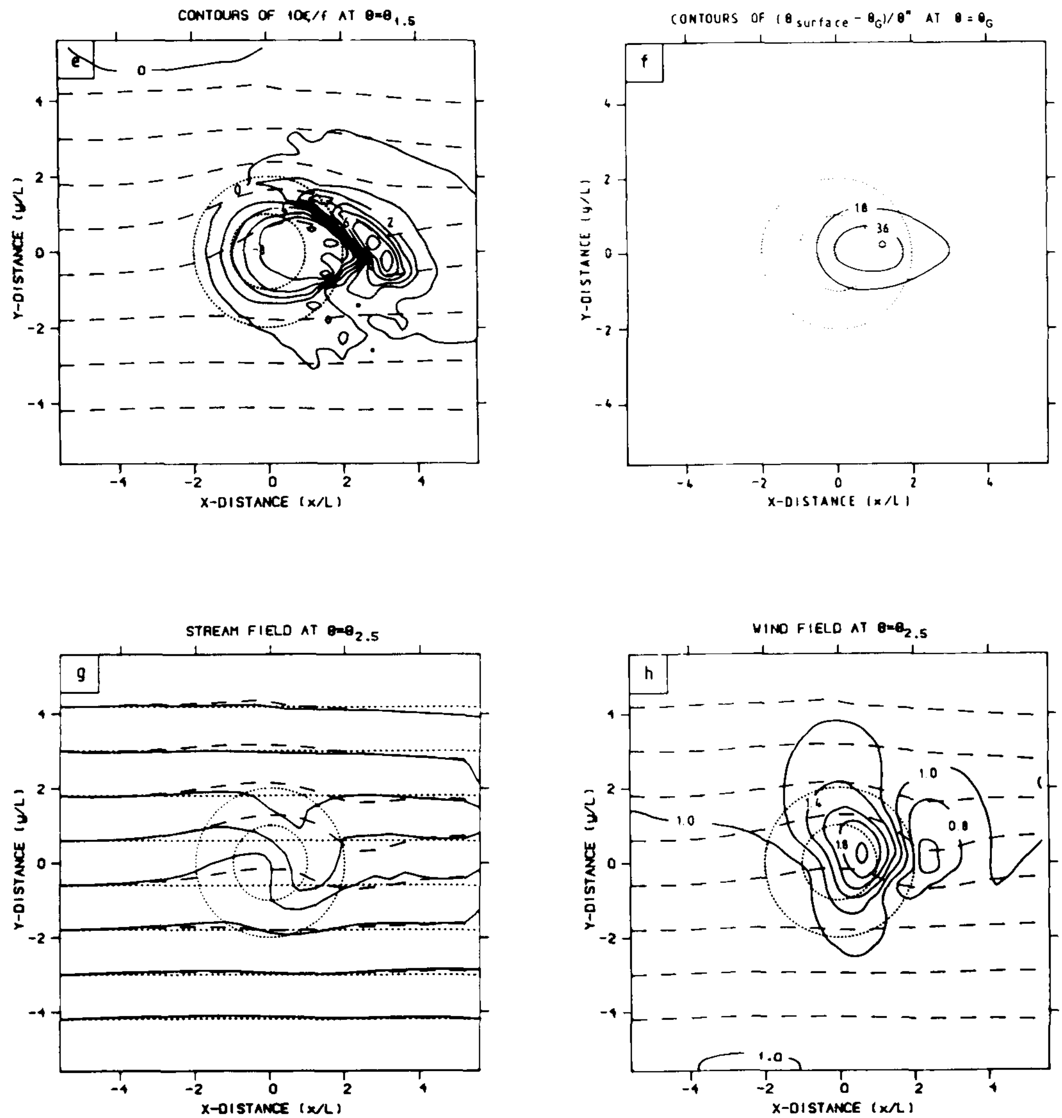

Fig. 6. (Continued.)

$\theta^* = 1/6$ these ϑ-values correspond to 3, 6, 9 and 12°K, respectively. The markers in the figure indicate the actual values of (H, ϑ) for the set of simulations used. From the values of Ro = 0.4, 1.0 and 4.0 we can see the maximum magnitude of collapse of θ-surfaces increases for constant values of H with increasing Ro, and also for constant values of Ro with increasing H. These values can be compared with the collapse condition of Smith (1980). Smith found that collapse starts at $H = 1/2$ for the Ro $= \infty$ case. This value is indicated by the symbol x in Fig. 9. One might expect that the collapse for finite Rossby numbers starts at a larger H value. The condition given by Smith is in fair agreement with the above results.

Fig. 10 shows the non-dimensional downstream extent, x_s, of the collapse region at the

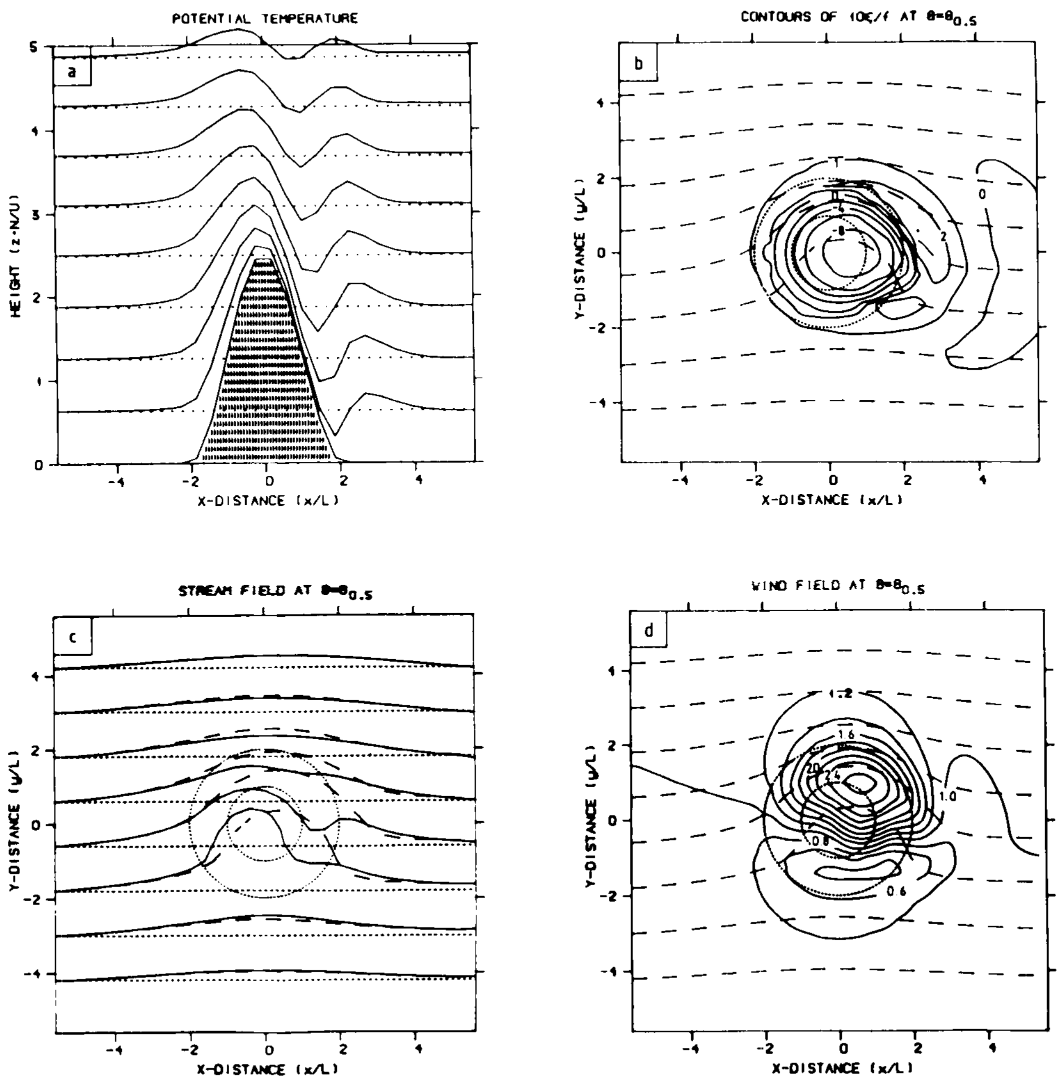

Fig. 7. Experiment 3. Results for flow past an isolated circular mountain (eq. (5.1)) with $H = 2.5$ and $\mathrm{Ro} = 0.4$. Explanation: (a)–(d) as in Fig. 5.

ground surface as a function of Ro and H (with S fixed). This extent is subjectively evaluated. For $\mathrm{Ro} = 0.4$ and 1.0, the downstream extent of collapse increases somewhat faster than linearly with increasing RoH, such that for a large H the extent is somewhat larger than the radius of deformation Nh_m/f. In order to investigate the collapse feature in a case with $H \geqslant 2$ and $\mathrm{Ro} \geqslant 2$, it would be desirable to perform the integration for a region with a considerably larger downstream extent.

6. Concluding remarks

Solutions have been presented for the inviscid, adiabatic primitive equations which exhibit quasi-stationary nature of flow over bell-shaped

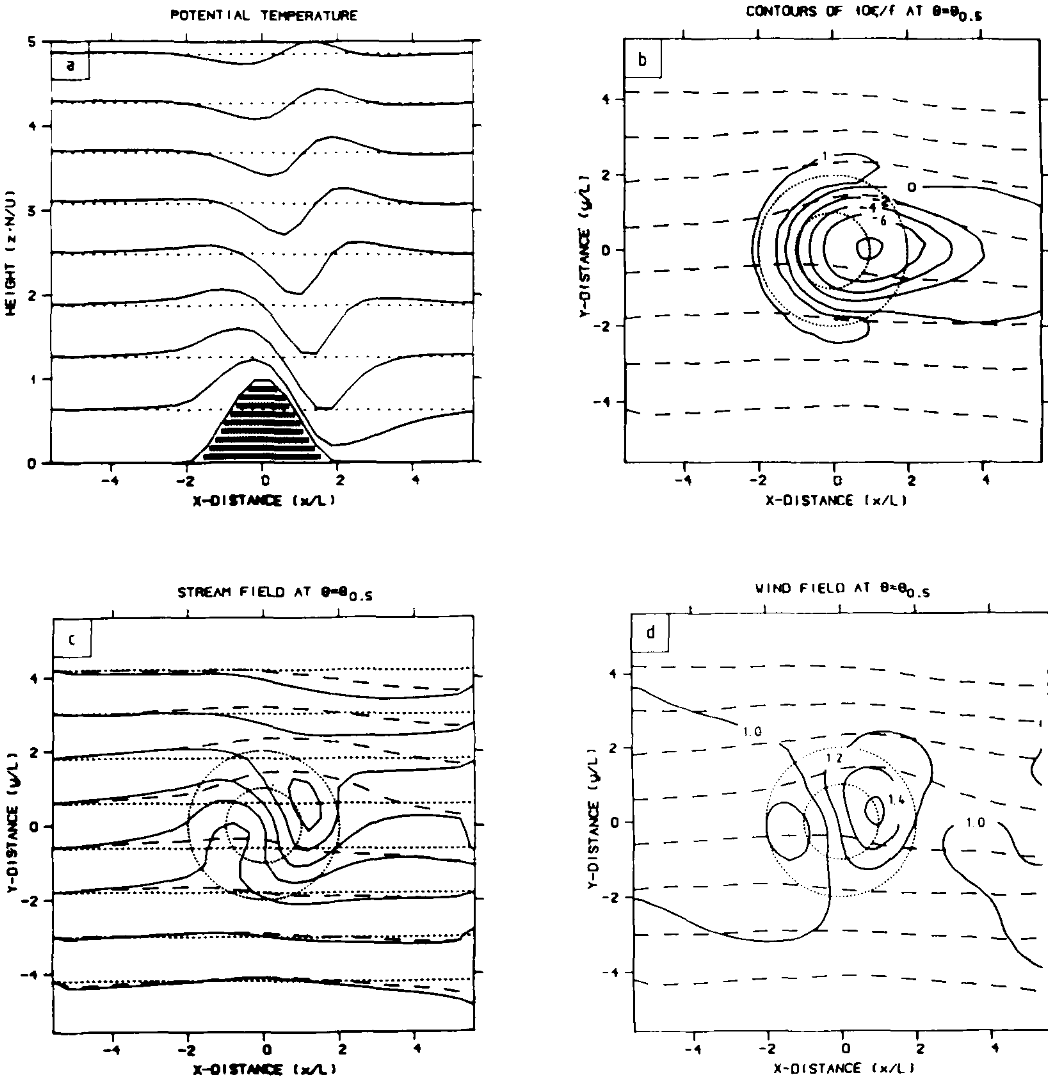

Fig. 8. Experiment 4. Results for flow past an isolated circular mountain (eq. (5.1)) with $H = 1.0$ and $\mathrm{Ro} = 4.0$. Explanation: (a)–(d) as in Fig. 5.

isolated mountains on the rotating earth. The controlling parameters are found to be the three non-dimensional numbers $S = (NU/g)^2$, $\mathrm{Ro} = U/fL$ and $H = Nh_m/U$. In these experiments N and U are kept constant. Thus, the investigation has dealt with the nature of the mountain flow in relation to the parameters Ro and H with a fixed S. This study suggests that for a sufficiently large Ro and H most of the low level air is diverted around the mountain, and the downslope flow on the lee side originates from potentially warmer upwind strata above the surface. For $\mathrm{Ro} \gg 1$, one must assume that the earth's rotation has little effect and the low-level flow is nearly symmetric with respect to the central streamline. With decreasing Ro, the low-level flow shows increased asymmetry, and for not too small a value for H, most of the low-level

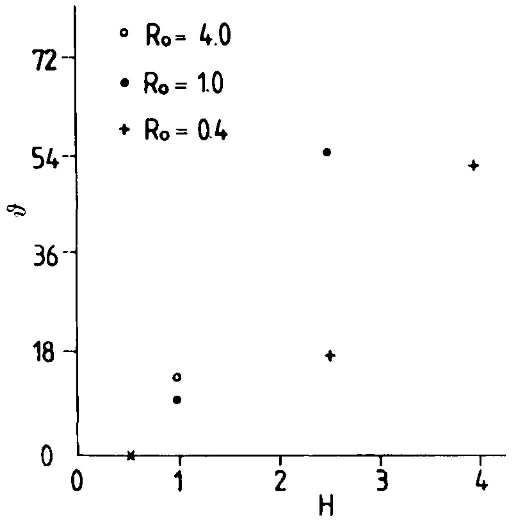

Fig. 9. Maximum magnitude of collapse of θ-surfaces at ground surface as function of Ro and H. Value $H = 0.5$ for start of collapse in the Ro $= \infty$ case (Smith, 1980) is indicated by "x".

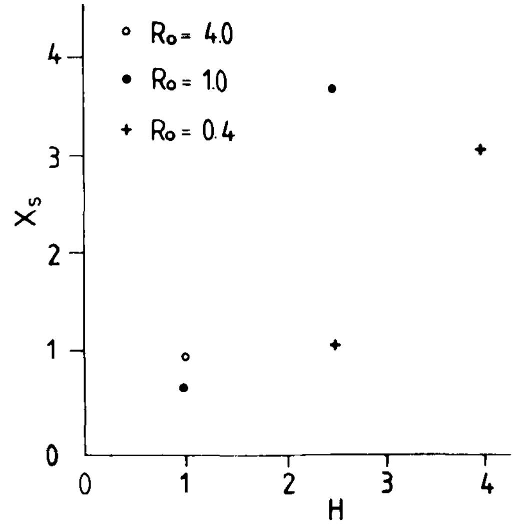

Fig. 10. Downstream extent of warm collapse zone at ground surface as a function of H, for Ro = 0.4, 1.0 and 4.0.

flow passes on the left side of the mountain (Northern Hemisphere). The maximum magnitude of the collapse of θ-surfaces occurs at the upper part of the lee slope. This maximum increases for constant values of H with increasing Ro, and also for constant values of Ro with increasing H. The downstream extent of the increased potential temperature zone is of the order of Nh_m/f. The location of the minimum and maximum wind speeds is most sensitive to the value of Ro, and their strength is most sensitive to H.

The isentropic model used in this study specifies potential vorticity as a function of its potential temperature. This property allows steady solutions to be found with an efficient numerical scheme. The numerical divergent diffusion may have reduced the collapse of θ-surfaces.

7. Acknowledgements

The major part of this work was done at Institute of Geophysics at the University of Oslo. It was supported by the Icelandic Fire Insurance Company, the Icelandic Science Foundation and the Nordic Council of Ministers. The Norsk Data Iceland gave access to a text processing system. The majority of these results were presented as part of my Dr. Scient. work at the University of Oslo in 1986. I wish to thank my supervisor, Prof. Arnt Eliassen, for encouragement and invaluable discussions during all stages of this investigation. Thanks also go to Mr. Arne M. Bratseth and Prof. Ronald B. Smith for their advice and criticism.

8. Appendix: List of symbols

A	damping coefficient
A_1, A_2	constant values of A
c_g	group velocity
c_p	$= 1004$ m^2 s^{-2} K^{-1} specific heat capacity at constant pressure
f	Coriolis parameter
g	$= 9.8$ m s^{-2} acceleration of gravity; suffix indicating geostrophic
G	suffix indicating lower boundary
h	shape and location of mountain
h_m	height of mountain
H	$= Nh_m/U$
k	numbering of θ-surfaces ($k = 0$ at the ground)
L	half width of circular mountain
m	$= gz + \theta\Pi(p)$ Montgomery potential; m_1 and m_2 defined in Section 2
M	initial equilibrium values of m

n	time index
N	buoyancy frequency
p	pressure
P	initial equilibrium values of p
q	potential vorticity
R	$= 287$ m^2 s^{-2} K^{-1} specific gas constant
Ro	$= U/fL$ Rossby number
S	$= (NU/g)^2$ non-dimensional stability
t	time
T	temperature; suffix indicating upper boundary
u, v	Cartesian components of horizontal velocity
U	initial equilibrium values of u
x, y	horizontal Cartesian coordinates
x_s	downstream extent of the collapse region
z	height
Z	$= f + \xi = f + \partial v/\partial x - \partial u/\partial y$
α	height growth of the mountain
β	coefficient in estimate of phase speed
$\delta_x, \delta_y, \delta_t$	centred finite differences
$\eta(x, y)$	lateral trajectory displacement
$\eta_g(x, y)$	geostrophic trajectory displacement
ζ	vertical trajectory displacement
θ	$= c_p T/\Pi(p)$ potential temperature
θ^*	$= c_p/U^2$ unit for potential temperature
θ_G	constant potential temperature of the lowest isentropic surface coinciding with the ground
$\theta_{surface}$	potential temperature of the highest isentropic surface in contact with the ground
ϑ	$= \max((\theta_{surface} - \theta_G)/\theta^*)$
κ	horizontal diffusivity coefficient
μ	Rayleigh friction coefficient
ξ	relative vertical vorticity
$\Pi(p)$	$= c_p(p/1\ \text{bar})^{R/c_p}$ Exner function
$\overline{(\ )}^x, \overline{(\ )}^y, \overline{(\ )}^\theta \overline{(\ )}^t$	average over one grid mesh

REFERENCES

Atkinson, B. W. 1981. Downslope winds. In *Meso-scale atmospheric circulations*. London: Academic Press, 80–108.

Bleck, R. 1979. Finite difference equations in generalized vertical coordinates. Part II: Potential vorticity conservation. *Beitr. Phys. Atmos. 52*, 95–105.

Charney, J. and Stern, M. E. 1962. On the stability of internal baroclinic jets in a rotating atmosphere. *J. Atmos. Sci. 19*, 159–172.

Eliassen, A. 1980. Balanced motion of a stratified, rotating fluid induced by bottom topography. *Tellus 32*, 537–547.

Eliassen, A. and Rekustad, J. E. 1971. A numerical study of mesoscale mountain waves. *Geofys. Publ. 28-3*, 1–13.

Eliassen, A. and Thorsteinsson, S. 1984. Numerical studies of stratified air flow over a mountain ridge on the rotating earth. *Tellus 36A*, 172–186.

Hogg, N. G. 1980. Effects of bottom topography on ocean currents. *GARP Publ. Series 23*, 167–205.

Kurihara, Y. and Bender, M. A. 1983. A numerical scheme to treat the open lateral boundary of a limited area model. *Mon. Wea. Rev. 111*, 445–454.

Orlanski, I. 1976. A simple boundary condition for unbounded hyperbolic flows. *J. Comput. Phys. 21*, 251–269.

Pierrehumbert, R. T. 1984. Linear results on the barrier effects of mesoscale mountains. *J. Atmos. Sci. 41*, 1356–1367.

Pierrehumbert, R. T. and Wyman, B. 1985. Upstream effects of mesoscale mountains. *J. Atmos. Sci. 42*, 977–1003.

Queney, P. 1947. Theory of perturbations in stratified currents with applications to airflow over mountain barriers. Misc. Report No. 23, Dept. of Met., Univ. of Chicago, 81 pp.

Queney, P. 1973. Transfer and dissipation of energy by mountain waves. In *Dynamic meteorology* (ed. P. Morel). Dordrecht/Holland: D. Reidel Publ. Comp., 513–617.

Ross, B. B. and Orlanski, I. 1982. The evolution of an observed cold front. Part I: Numerical simulation. *J. Atmos. Sci. 39*, 296–327.

Sadourny, R. 1975. The dynamics of finite-difference models of the shallow-water equations. *J. Atmos. Sci. 32*, 680–689.

Shapiro, R. 1970. Smoothing, filtering, and boundary effects. *Rev. Geophys. Space Phys. 8*, 359–387.

Smith, R. B. 1980. Linear theory of stratified hydrostatic flow past an isolated mountain. *Tellus 32*, 348–364.

Smith, R. B. 1982. Synoptic observations and theory of orographically disturbed wind and pressure. *J. Atmos. Sci. 39*, 60–70.

Somieski, F. 1981. Linear theory of three-dimensional flow over mesoscale mountains. *Beitr. Phys. Atmos. 54*, 315–334.

Vergeiner, I. 1978. Foehn flow in the Alps—Three-dimensional numerical simulations on the small- and mesoscale. *Arb. Zentral. Meteorol. Geodyn. Wien, No. 31*, 1–30.